RESEARCH ARTICLE

A Feasibility Study of Land CSEM Surveys With a Near-Casing Source for Hydraulic Fracturing Monitoring

YAO LU [1,3], **HANDONG TAN** [1], **DIKUN YANG** [2], **ZHIGANG WANG** [3], **YUNJIAN YANG** [3], **LIANGJUN YAN** [4], **WEI WAN** [5], **AND HANBING WANG** [1]

[1] School of Geophysics and Information Technology, China University of Geosciences, Beijing 100083, China
[2] Department of Earth and Space Sciences, Southern University of Science and Technology, Shenzhen 518055, China
[3] BGP Inc., CNPC, Zhuozhou 072750, China
[4] Key Laboratory of Exploration Technologies for Oil and Gas Resources, Yangtze University, Wuhan 430100, China
[5] School of Geophysics and Measurement-Control Technology, East China University of Technology, Nanchang 330013, China

Corresponding authors: Handong Tan (thd@cugb.edu.cn) and Dikun Yang (yangdikun@gmail.com)

ABSTRACT The land controlled-source electromagnetic (CSEM) method dynamically monitors reservoir fluid by contrasting electrical conductivity between hydraulic fracturing fluids and surrounding rock formations. In hydraulic fracturing monitoring, the underground steel casings represent significant high-conductivity objects that require accurate and rapid numerical modeling for understanding the CSEM responses and optimizing the survey configurations. To efficiently simulate the steel well casings, we made use of the modified finite volume method (FVM) with the concept of edge conductivity equivalence that avoids the computational cost of grid refinement down to millimeters or centimeters for the casing. The new algorithm is satisfactorily validated by a numerical comparison against a trusted program Dipole1D and a commercial program COMSOL. Then the algorithm is used to investigate the characteristic CSEM responses of injected fracturing fluid due to a galvanic electromagnetic (EM) source grounded near the head of steel-cased well, an unconventional configuration that can maximize the data anomaly by channeling more excitation current to the deep reservoir. In particularly, we simulated two fracturing scenarios with different fluid migration directions: one with a high-resistivity cap layer as the background and the other with a realistic heavy oil fracturing site from Karamay in Xinjiang, China. Our simulation shows that the configuration of near-casing excitation significantly enhances the electric-field anomalies of the fluid injection, which is the most prominent as the galvanic effect at low frequencies. These phenomena highlight the crucial role of steel casing in the CSEM method for hydraulic fracturing monitoring.

INDEX TERMS Controlled-source electromagnetic, casing well, finite volume method, hydraulic fracturing monitoring.

I. INTRODUCTION

The controlled-source electromagnetic (CSEM) method in the frequency domain is a vital geophysical technique for probing subsurface electrical structures [1], [2], [3],

The associate editor coordinating the review of this manuscript and approving it for publication was Leung Tsang.

[4]. In recent years, advances in CSEM instruments and data processing have significantly improved the quality and efficiency of data collection, providing a foundational dataset for detailed 3D subsurface electrical structures [5]. With the widening application of hydraulic fracturing technology, the exploration of new methods for dynamic hydraulic fracturing monitoring has become a research focus.

Time-lapse geophysical methods, as effective approaches for dynamic hydraulic fracturing monitoring, are gradually finding applications and demonstrating promising outcomes [6], [7], [8]. Seismic technology, the most developed time-lapse geophysical method [9], [10], widely applied in identifying rock fracturing induced by hydraulic fracturing. It faces challenges in identifying the fracturing fluids within natural subsurface fractures. However, the injection of fracturing fluid during hydraulic fracturing induces changes in the electrical properties of the formation, laying the geophysical groundwork for utilizing the CSEM method for hydraulic fracturing monitoring. It is worth noting that in hydraulic fracturing monitoring using the CSEM method, the substantial electrical conductivity contrast between underground steel casings and the formation leads to current diffusion across boreholes, significantly distorting the electromagnetic signals collected by the receivers [11]. Therefore, prior to employing the CSEM method for hydraulic fracturing monitoring, it is essential to use numerical simulation methods to study the EM response characteristics of steel casings.

Although the impact of steel casings on EM signals is not a new issue in geophysics, conducting efficient 3D numerical simulations that account for steel casings remains a challenging problem. Among various studies, some researchers discretize steel casings at a millimeter-scale grid resolution and employ numerical algorithms to achieve detailed simulations of arbitrarily complex 3D models at the cost of computational efficiency [12], [13], [14], [15]. However, the implementation of this method in complex steel-casing systems poses significant challenges. To simultaneously consider computational efficiency and large-scale geological structural targets, researchers have used coarse grid cells of high conductivity to approximate steel casings in numerical simulations [16], [17], [18], [19], [20], [21], [22] The forward modeling method based on equivalent sources achieves accurate calculations for variable surrounding rock and nonuniform distribution conditions. However, solving for source distribution requires a simple background, which can introduce computational errors in a complex environment. Other researchers have proposed treating the contact between steel casings and the earth as a unique boundary condition, omitting the casing's structure and resistivity [23], [24]. This method involves treating shorter steel casings as equipotential or highly conductive bodies using unstructured mesh techniques for better computational efficiency. However, in realistic hydraulic fracturing scenarios, where steel casing lengths can extend for kilometers, the casing's electric potential deviates from the ideal equipotential state. Certainly, some scholars have improved the equivalent source method by employing a multiscale approach to mitigate errors caused by variations in the steel casing conductivity and grounding conditions [25], [26]. Other scholars have achieved rapid computation of the direct current responses of the steel casing within the grid by improving the conductivity parameters of the nodes, thereby eliminating the need for grid refinement [27]. Certain scholars have employed edge

conductivity to model steel casings and deep learning for fracturing fluid imaging [28], [29], [30]. This approach does not require additional degrees of freedom to represent the intricate geometry of the casing, thereby notably improving the efficiency of 3D simulations in steel casing fracturing models. Although the various methods described above demonstrate electromagnetic anomalies caused by hydraulic fracturing, we still lack a proper understanding of multicluster fracturing as the primary target. Numerous studies have shown that utilizing a steel casing as a long electrode can enhance the effectiveness and sensitivity of CSEM monitoring for hydraulic fracturing; however, in real application scenario, transmitting a large current directly through the well casing is mostly impossible. As a result, it becomes necessary to quantitatively evaluate the effectiveness of the near-casing configuration, which is a practical alternative to the long electrode method, in which the current source is grounded at a small distance from the well head.

FVM has been widely applied in various applications such as geothermal, hydrocarbon, and minerals exploration to solve the 3D CSEM problems in both marine and terrestrial environments. This study was based on the FVM, employing the edge conductivity equivalent method [28] for 3D forward modeling of the land CSEM method with steel casing wells and a near-casing source. First, we derived a finite-volume 3D forward modeling algorithm and introduced the edge conductivity equivalent method. Then, we tested the code with synthetic examples to confirm its validity and discuss the effects of the steel casing on the forward results. Finally, we applied the algorithm to the high-resistivity cap layer model and the realistic heavy oil hydraulic fracturing model with steel casing, analyzing the anomalies in the surface electric-field data caused by fluid injection and migration in multi-cluster fracturing.

II. METHOD
A. FORWARD
The frequency-domain CSEM method belongs to the typical low-frequency electro-magnetic method where, within most known ranges of resistivity in the earth medium, displacement currents can be disregarded. The differential form of the frequency-domain Maxwell's equations (considering the time-harmonic factor as $e^{i\omega t}$) is as follows:

$$\nabla \times \boldsymbol{H} = \sigma \boldsymbol{E} + \boldsymbol{J}_s \tag{1}$$

$$\nabla \times \boldsymbol{E} = -i\omega\mu_0 \boldsymbol{H} \tag{2}$$

where $\boldsymbol{E}$ is the electric field, $\boldsymbol{H}$ is the magnetic field, $\boldsymbol{J}_s$ is the current density of the source, i is an imaginary unit, ω is the angular frequency, μ_0 is the permeability of free space, and σ is the electrical conductivity.

Combining (1) and (2) to eliminate the magnetic field term, we obtain the curl-curl equation for the electric field:

$$\nabla \times \nabla \times \boldsymbol{E} + i\omega\mu_0\sigma \boldsymbol{E} = -i\omega\mu_0 \boldsymbol{J}_s \tag{3}$$

In our approach to solving (3), we utilize the FVM and employ Yee's staggered grid for spatial discretization of the
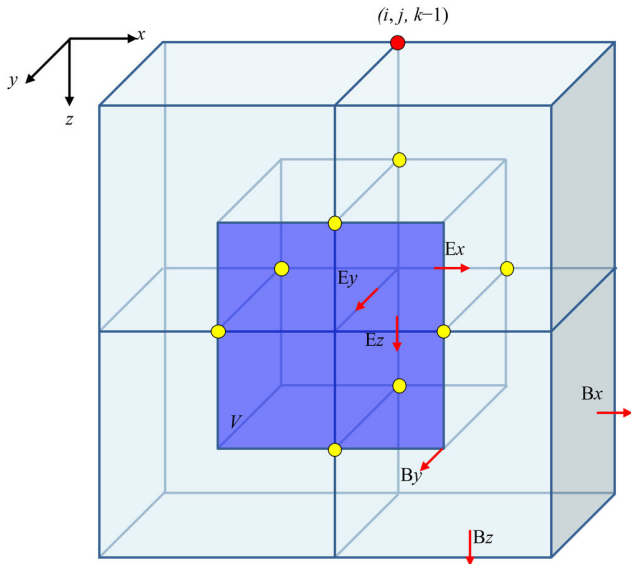
FIGURE 1. Schematic representation of the control volume for the Ey component at a sampling point in the Yee grid.

electromagnetic field. Specifically, the electric field was positioned at the mesh edges, whereas the magnetic field was situated at the centers of the mesh faces. The finite volume method (FVM) partitions the computational domain into a series of control volumes, ensuring that each sampling point is surrounded by a control volume. This method involves integrating the differential equations over each individual control volume. For any given sampling point, (3) is integrated over the control volume Ω as follows:

$$\int_{\Omega} \nabla \times \nabla \times E d\Omega + i\omega\mu_0 \int_{\Omega} \sigma E d\Omega = -i\omega\mu_0 \int_{\Omega} J_s d\Omega \tag{4}$$

According to the Gauss divergence theorem, (4) can be transformed as follows:

$$\int_{\Gamma} \boldsymbol{n} \times (\nabla \times \boldsymbol{E}) \, d\Gamma + i\omega\mu_0 \int_{\Omega} \sigma E d\Omega = -i\omega\mu_0 \int_{\Omega} J_s d\Omega \tag{5}$$

where $\boldsymbol{n}$ represents the outward unit normal vector to the surface Γ.

Taking the Ey component at an arbitrary sampling point as an example, the concept of control volumes within the framework of the finite-volume method was elucidated [31].

The dark-shaded volume region in Fig. 1 represents the control volume V centered around Ey. We could readily obtain the control volumes for the Ex and Ez component at the same sampling point.

Integrating (5) within the control volume depicted in Fig. 1, the conductivity at a specific sampling point can be obtained by the volume-weighted average of the conductivity of the four adjacent mesh elements sharing the sampling point along the edge. Because the steel casing has a cross-sectional area that is significantly smaller than the large-scale grid elements

of the subsurface medium, when the steel casing coincides with the edges, it can be assumed that the conductivity of the steel casing only exists along the edges. Therefore, when performing volume-weighted conductivity averaging, the weighted volumes of the four adjacent elements remained unchanged. The new relationship for average conductivity can be expressed as follows [11]:

$$\begin{aligned}(V_1 + V_2 + V_3 + V_4 + V_5) \cdot \tilde{\sigma} \cdot \tilde{E} \\ = V_1 \cdot \sigma_1 \cdot \boldsymbol{E}_1 + V_2 \cdot \sigma_2 \cdot \boldsymbol{E}_2 + V_3 \cdot \sigma_3 \cdot \boldsymbol{E}_3 \\ + V_4 \cdot \sigma_4 \cdot \boldsymbol{E}_4 + V_5 \cdot \sigma_5 \cdot \boldsymbol{E}_5\end{aligned} \tag{6}$$

where V denotes the volume of the conductive body, subscripts 1–4 represent the four rectangular prisms, and the subscript 5 represents the steel casing.

Typically, assuming minimal variation in the electric field within the control volume, we can derive the average conductivity within the control volume by neglecting the changes in the electric field as follows:

$$\tilde{\sigma} = \frac{\sum_{k=1}^{5} V_k \sigma_k}{V_1 + V_2 + V_3 + V_4} \tag{7}$$

The right-hand side of (5) represents the integration of the current density within the control volume. The long conductive wire sources utilized in hydraulic fracturing monitoring can be decomposed into superposition of electric dipole sources. Any dipole source in a specific direction is divided into x, y, and z components. Each component is then distributed based on trilinear interpolation, onto the eight closest edges aligned in the respective directions.

Finally, applying Dirichlet boundary conditions to the grid elements on the boundary involves setting the tangential components to zero, resulting in the formulation of a complex symmetric equation set.

$$\boldsymbol{KE} = \boldsymbol{b} \tag{8}$$

where E is a vector representing the discrete electric field values on the mesh edges, b is the discretized right-hand side, and K is the coefficient matrix.

We employed the direct solver PARDISO to solve (8), enabling us to obtain the electric field values on the edges of the grid. The electric field at arbitrary points can be obtained by trilinear interpolation from the edge electric field, whereas the magnetic field can be computed by differencing (2).

B. VALIDATION

In this section, we first use a semi-analytic solution, Dipole1D [32] (Key, 2009) for 1D layered resistivity models to validate the accuracy of our modified FVM 3D forward modeling. Vertical and "L"-shaped steel casing configurations are common underground metallic structures used in hydraulic fracturing well sites. Compared with the surrounding rock formations, these configurations exhibit higher electrical conductivity, smaller cross-sectional dimensions, and longer extension lengths, causing distortions in the observed EM field around the well on the surface. To further validate the accuracy of our algorithm for 3D models

with vertical and "L"-shaped steel casings, we compared our results with COMSOL. These programs were executed on a Linux cluster with each node having 256G RAM and 32 cores running at 2.5 GHz.

1) MODEL 1: 1D LAYERED MODEL

The model comprised three layers with the following conductivities: 0.02 S/m and 1000 m thickness for the first layer, 0.01 S/m and 1000 m for the second layer, and 0.005 S/m for the third layer. The conductivity of the air layer was 1×10^{-7} S/m. Along the surface in the X-direction, a 100 m horizontal electric dipole source was positioned with positive electrode A located at $(-100, 0, 0)$ m and negative electrode B at $(-200, 0, 0)$ m. Our simulations used 1 A current at three frequencies: 0.01 Hz, 1 Hz, and 100 Hz. The surface X-component electric field receivers were distributed along the line $y = 0$ m between $x = 0$ m and $x = 2000$ m, uniformly spaced at 100 m. For the 3D FVM forward modeling, the rectilinear mesh contained 437,060 cells. We used FVM and Dipole1D to calculate the X-component electric field amplitudes (E_x^{amp}) of the receivers and compared their relative errors.

Fig. 2 shows the FVM numerical solutions along with the Dipole1D semi-analytical solutions of E_x^{amp} and the relative errors at 0.01 Hz, 1 Hz, and 100 Hz. It is evident that the FVM solutions agree well with the semi-analytical solutions with relative errors below 2%. This confirms the correctness and accuracy of the basic FVM 3D forward model, validating its applicability to more complex models and further numerical experiments.

2) MODEL 2: 3D MODEL WITH VERTICAL STEEL CASING

We used a 200 m $\times$ 200 m horizontal slab that was 1 m thick and in a constant conductivity of 0.01 S/m as the anomalous object. The slab was buried 500 m beneath the ground surface in a 1 S/m half-space background (Fig. 3 (a)). The air layer had a conductivity of 1×10^{-7} S/m. A 600 m-long vertical casing with the wellhead at $(0, 0, 0)$ m intersects the center of the anomaly and has an intrinsic conductivity of 1×10^{7} S/m with inner and outer diameters of 0.16 m and 0.21 m, respectively. A 100 m long horizontal electric dipole source was placed on the surface with electrode A at $(-50, 0, 0)$ m and electrode B at $(-150, 0, 0)$ m. The source transmitted a current of 1A at 2 Hz. The surface X-component electric field receivers were distributed along the line $y = 0$ m between $x = 30$ and 500 m and were uniformly spaced 10 m apart. The equivalent edge conductivity of the steel casing was calculated to be 1.5×10^{5} S/m throughout the entire well path, although this value can be variable in a realistic field survey. In 3D forward modeling, the total number of mesh cells employed was 526,500. We employed the FVM algorithm and COMSOL to compute E_x^{amp} at each receiver and subsequently determined the relative error between the two methods. When simulating with COMSOL, we employed an unstructured mesh and accurately modeled the shape of the steel casing.

The FVM 3D forward modeling results shown in Fig. 3 (b) demonstrate excellent consistency with COMSOL. The relative errors between the results obtained from the two methods were within the range of -1.8% to $+1.8\%$. When a small cross-section, high-conductivity vertical steel casings are present underground, the E_x^{amp} results computed using the FVM proposed in this study are reliable. The simulation results validated the accuracy of the FVM 3D forward modeling algorithm in computing the results for 3D models incorporating vertical steel casings. The COMSOL simulation took approximately one and a half hour of computing time for the single steel-cased well and consumed 176 GB of RAM. The FVM took less than nine minutes.

3) MODEL 2: 3D MODEL WITH "L"-SHAPED STEEL CASING

In this model, the air conductivity was 1×10^{-7} S/m, whereas the background conductivity was 0.002 S/m (Fig. 4). A block anomaly with a conductivity of 1 S/m is observed. The center of the block is at the coordinates $(540, 60, -990)$ m, and the dimensions of the block were 400 m $\times$ 200 m $\times$ 200 m. The underground "L"-shaped steel casing has an inner diameter of 0.16 m, an outer diameter of 0.21 m, and a conductivity of 1×10^{7} S/m. The vertical section of the steel casing was 1000 m in length, starting at $(0, 0, 0)$ m and ending at $(0, 0, -1000)$ m. The horizontal section of the steel casing extends 800 m, starting at coordinates $(0, 0, -1000)$ m and ending at coordinates $(800, 0, -1000)$ m. The 1000 m-length horizontal electrical dipole source, with electrodes A $(-100, 0, 0)$ m and B $(-1100, 0, 0)$ m, carried a 1 A current at a frequency of 1 Hz. The surface X-component electric field receiver grid, uniformly spaced at 40 m, covers an area from 40 m to 1000 m in the X-direction and from -500 m to 500 m in the Y-direction. An equivalent edge conductivity of 1.5×10^{5} S/m is assigned to the steel casing. A total of 649,800 mesh cells were used in the simulation. For this simulation, both the FVM algorithm and COMSOL were employed to calculate E_x^{amp} at each receiver and the relative errors between the two methods.

Fig. 5 (a-b) display E_x^{amp} results at each receiver computed using the two methods. It exhibits higher magnitudes near the transmitter and diminished with distance. The magnitude of E_x^{amp} ranged from 1×10^{-5} to 1×10^{-2} V/m. Fig. 5 (c) shows the relative error between the calculations obtained from FVM and COMSOL. Apart from the small region near the transmitter source, the overall relative error is less than 1.5%. The agreement between the FVM algorithm and COMSOL validates the correctness of our forward code under the 3D model with "L"-shaped steel casing. These results confirmed that our code is reliable and can be applied to more complex and realistic models for further testing.

Additionally, when the synthetic model described above did not contain an anomaly with a conductivity of 1 S/m, we conducted the same calculations and comparisons. The total number of mesh cells for this model was 559,550. From Fig. 6 (a-b), it is evident that the contour line distribution of E_x^{amp} follows a similar trend to that in Figure 5 (a-b), but
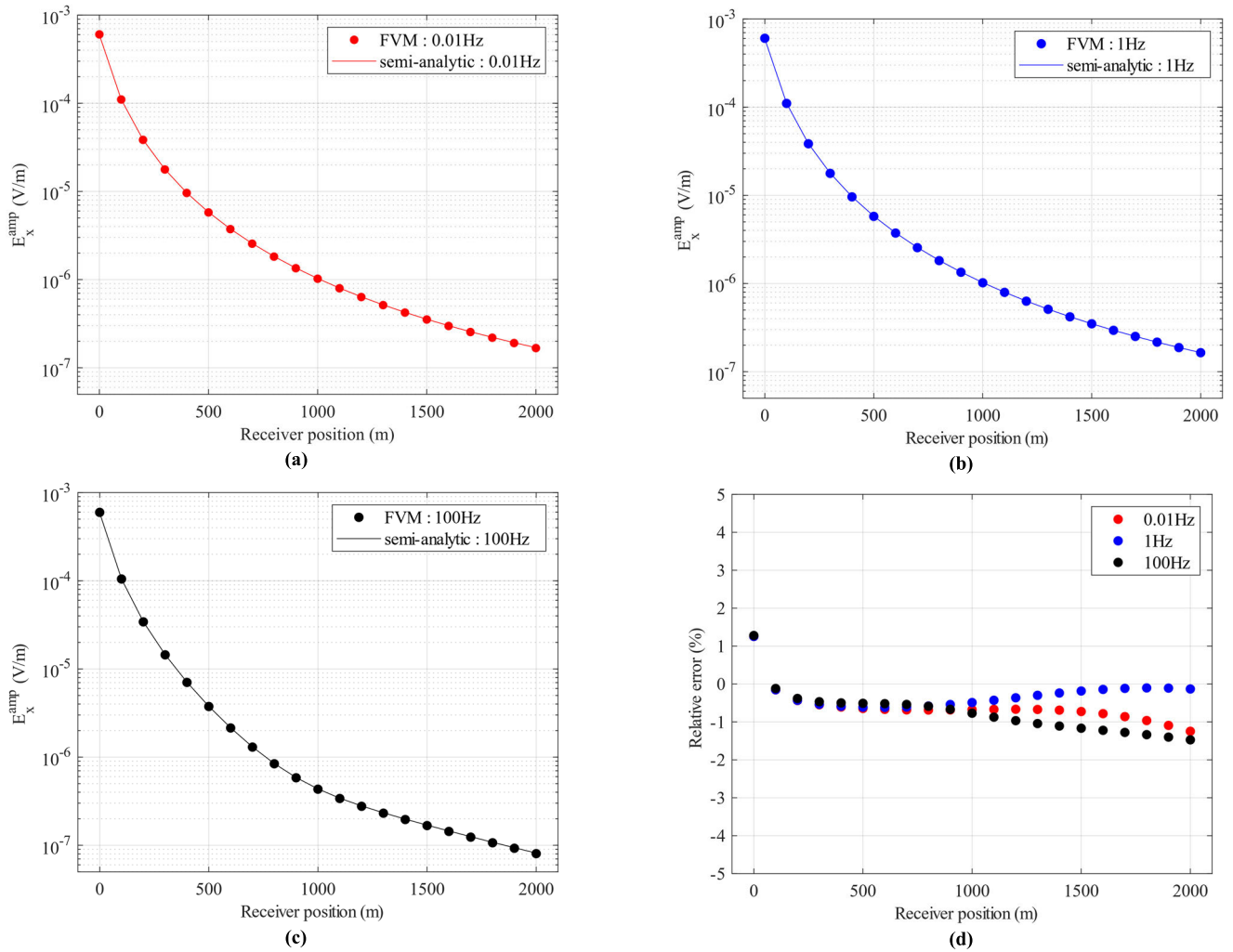
FIGURE 2. Accuracy verification for the 1D layered model. (a) E_x^{amp} at 0.01 Hz; (b) E_x^{amp} at 1 Hz; (c) E_x^{amp} at 100 Hz; (d) relative error between FVM-computed and Dipole1D-computed results at 0.01 Hz, 1 Hz, and 100 Hz [relative error $= 100 \times (E_{FVM} - E_{Dipole1D})/E_{Dipole1D}$].

the E_x^{amp} values at each receiver increased. This indicates that a subsurface anomaly with a conductivity of 1 S/m leads to a reduction in the amplitude of the surface X-component electric field. Fig. 6 (c) demonstrates that, except for a small region near the source, the relative error between the FVM and COMSOL for this model was less than 1.5%.

III. SYNTHETIC MODEL OF HIGH-RESISTIVITY CAP LAYER

The purpose of this model was to analyze the role of the steel casing in detecting the hydraulic fracturing fluid flow under a high-resistivity cap layer. First, this study calculated the pre-fracturing and post-fracturing E_x^{amp} at the surface receiver above the underground fracturing fluid. In addition, we simulated varying distances between a fixed-length transmitter and the wellhead to observe the different frequencies of E_x^{amp} and the relative difference. Ultimately, the relative difference of E_x^{amp} was computed at each receiver before and after the fracturing fluid migrated in four different directions.

Designing an appropriate underground fracturing fluid model based on the current hydraulic fracturing techniques is crucial for identifying fracturing fluids using the land CSEM method. Therefore, this study utilized three 3D ellipsoids arranged in parallel with identical shapes to approximate the morphology of the fracturing fluid of the three clusters in a single fracturing stage. As shown in Fig. 7 (a), a single ellipsoid model has semi-axis lengths of 40 m (x-axis), 160 m (y-axis), and 40 m (z-axis). The hydraulic fracturing fluids were assigned a uniform conductivity of 1 S/m. In the following context, pre-fracture refers to the absence of fracturing fluid in the model, whereas post-fracture indicates the presence of the three parallel arranged elliptical fracturing fluids. We calculated the relative difference in E_x^{amp} between pre-fracture and post-fracture as follows:

$$Relative\ Difference = \frac{100 \times (E_x^{Post\_Fracture} - E_x^{Pre\_Fracture})}{E_x^{Pre\_Fracture}}$$
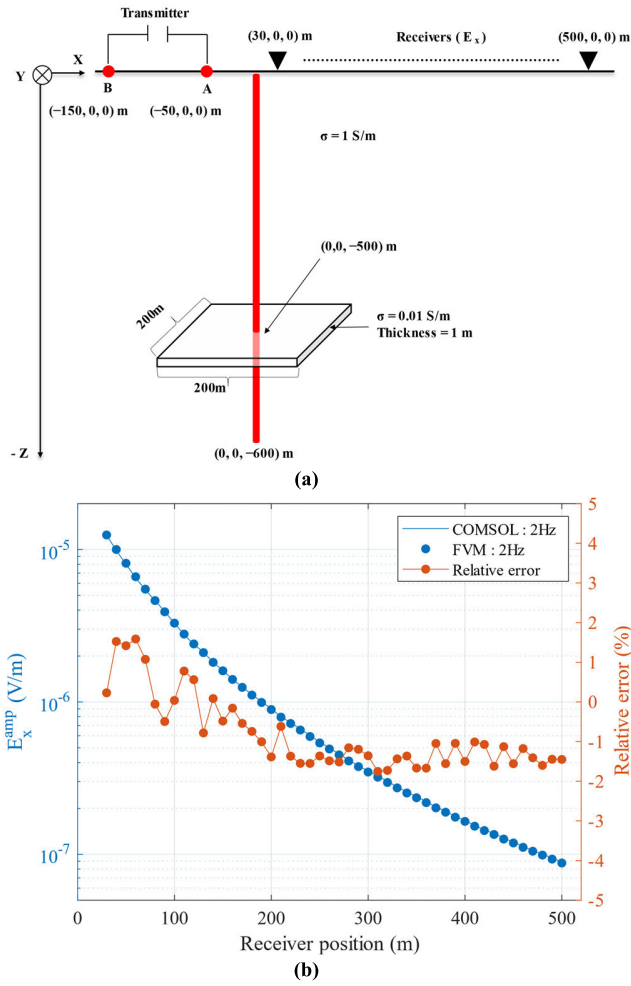
(9)

(a)

(b)

FIGURE 3. Accuracy verification for the 3D model with a vertical steel casing. (a) The 3D electrical model with a vertical steel casing marked in red; (b) The FVM and COMSOL simulation results of E_x^{amp} and the relative error at 2 Hz [Relative error $= 100 \times (E_{FVM} - E_{COMSOL})/E_{COMSOL}$].
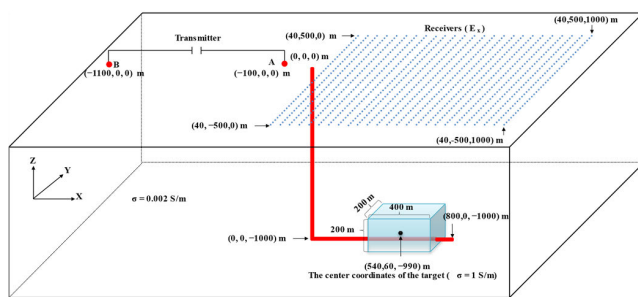

(a)

(b)

(c)

FIGURE 5. Accuracy verification for the 3D model with "L"-shaped steel casing [red curve] and block anomaly. (a) COMSOL simulation results at 1 Hz; (b) FVM simulation results at 1 Hz; (c) relative error between COMSOL and FVM at 1 Hz [Relative error $=100 \times (E_{FVM} - E_{COMSOL})/E_{COMSOL}$].

FIGURE 4. 3D model with "L"-shaped steel casing. The red line represents a steel-cased well.

where $E_x^{Post\_Fracture}$ is the E_x^{amp} of the post-fracture, and $E_x^{Pre\_Fracture}$ is the E_x^{amp} of the pre-fracture.

The high-resistivity cap layer model consists of three layers: the first layer with a conductivity of 0.1 S/m and a thickness of 200 m, the second layer with a conductivity of 0.001 S/m and a thickness of 500 m, and a third layer with a conductivity of 0.01 S/m. The region above the surface
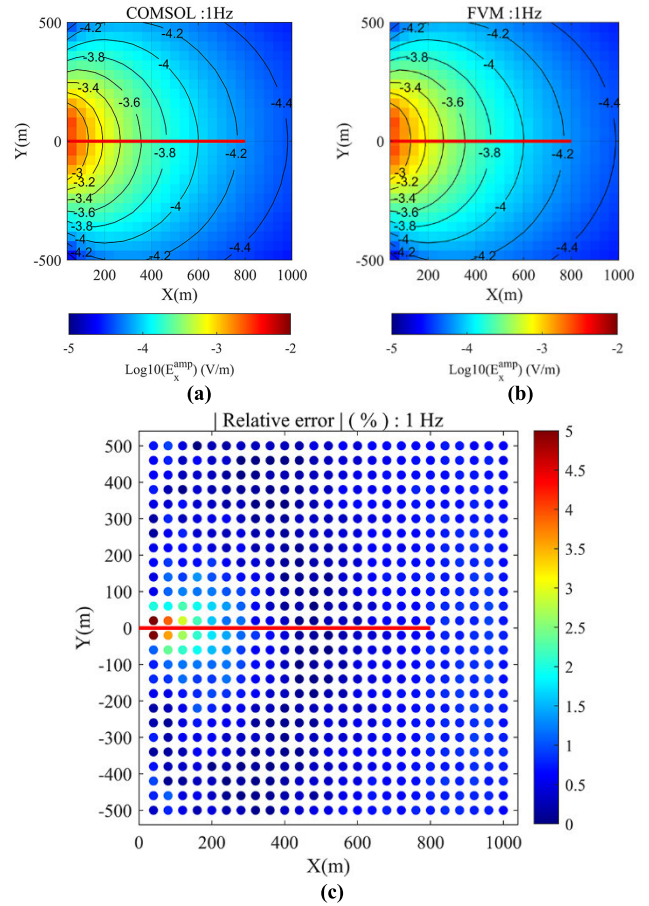
was air with a conductivity of 1×10^{-7} S/m. The centers of the three parallel arranged elliptical fracturing fluids are located at (460, 0, −1000) m, (500, 0, −1000) m, and (540, 0, −1000) m, respectively (Fig. 7 (a)). The length of the horizontal electric dipole source was 5000 m with a 1A current, utilizing electrode A at (−20, 0, 0) m and electrode B at (−5020, 0, 0) m. The receiver was located at (500, 0, 0) m. The steel casing has a conductivity of 1.5×10^5 S/m. There is a vertical section spanning 1000 m from (0, 0, 0) m to (0, 0, −1000) m and a horizontal section spanning 800 m from (0, 0, 1000) m to (800, 0, −1000) m. The model consists of 710,696 mesh cells. We computed the forward modeling results for 30 logarithmically spaced frequencies ranging from 0.01 Hz to 100 Hz.

Without the underground steel casing, the relative difference in E_x^{amp} between pre-fracturing and post-fracturing was below −0.025%, suggesting difficulty in effectively identifying the fracturing fluid at this size, as shown in Fig. 8 (c). The presence of an underground steel casing leads to a reduction in both the pre-fracture and post-fracture and post-fracture E_x^{amp} values. However, it also amplified the
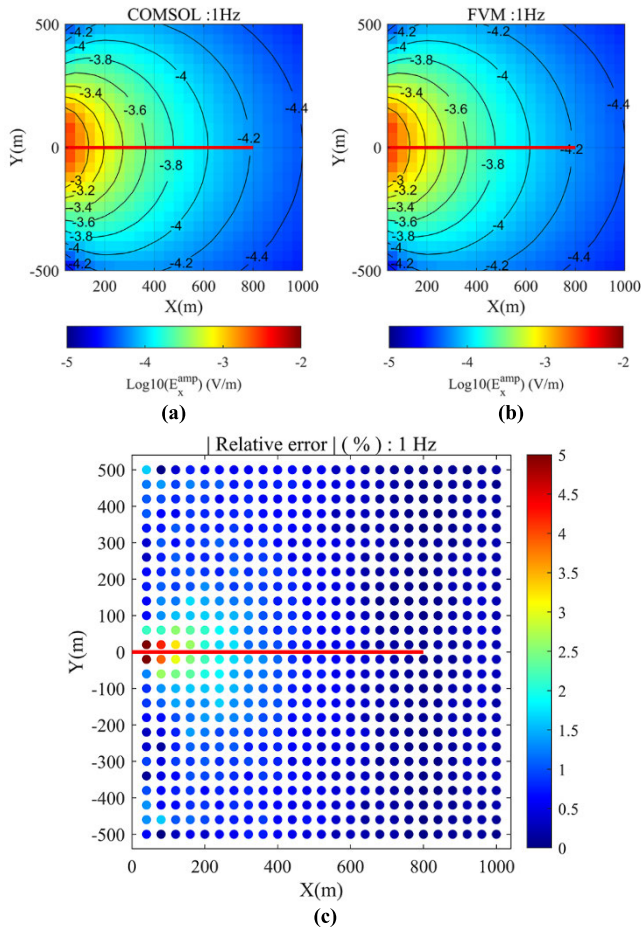
FIGURE 6. Accuracy verification for the 3D model with "L"-shaped steel casing [red curve] and block anomaly. (a) COMSOL simulation results at 1 Hz; (b) FVM simulation results at 1 Hz; (c) relative error between COMSOL and FVM at 1 Hz [Relative error $= 100 \times (E_{FVM} - E_{COMSOL})/E_{COMSOL}$].

difference between pre- and post-fracturing, resulting in a maximum relative difference of nearly -5.8%, as depicted in Fig. 8 (b). The results demonstrate that the underground steel casing facilitates the penetration of the source current through the high-resistivity cap layer, consequently increasing the relative difference in E_x^{amp}. Our simulation results also indicate that the fracturing fluid anomaly is the most prominent at low frequencies; in practice, we may choose the optimal frequency to be approximately 1 Hz or 2 Hz for a balance between the efficiency and signal-to-noise ratio (Fig. 8 (b)).

To research the relationship between the relative difference of E_x^{amp} and the distance from the transmitter to the wellhead, we placed a fixed set of wire sources at varying distances from the wellhead. The orientation and length of the transmitter remain constant, as shown in Fig. 7 (a). Because of the potential severe safety issues associated with the direct connection of the transmitter to the steel casing wellhead, a scenario in which the distance between transmitter electrode A and the wellhead is 0 m was not considered. The transmitter electrode A is initially positioned at $(-20, 0, 0)$ m and gradually moves
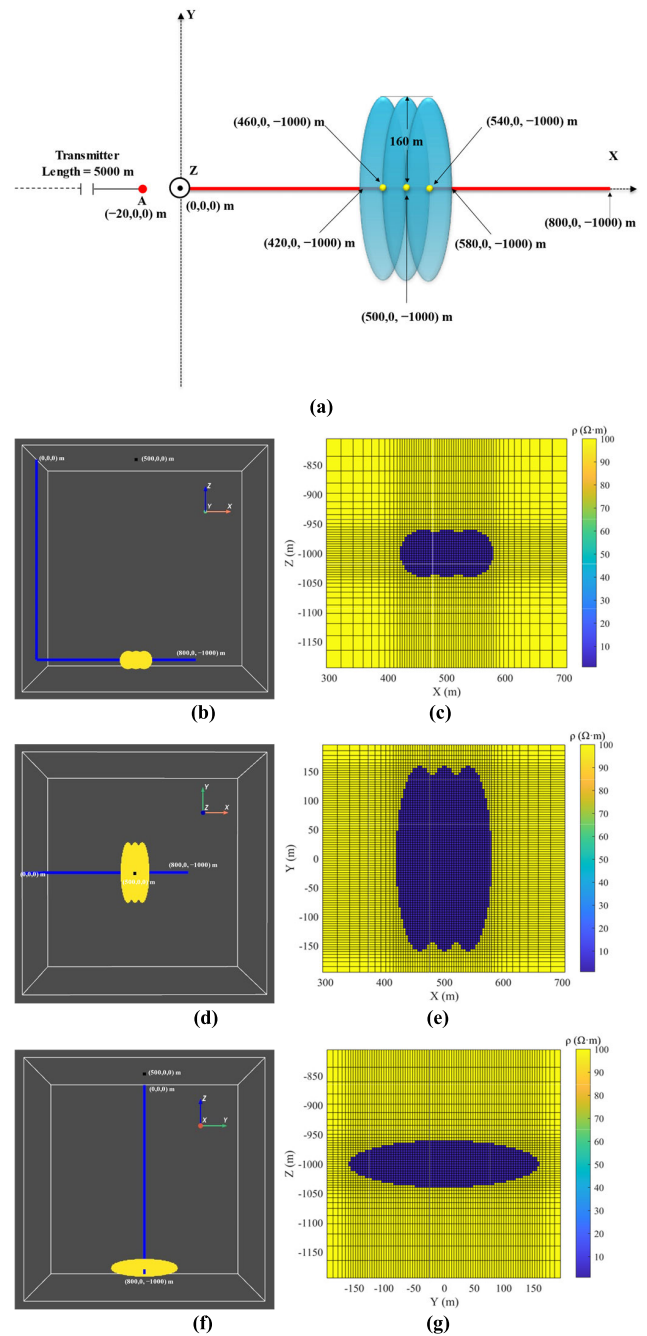

FIGURE 7. Synthetic model of high-resistivity cap layer with three parallel arranged elliptical fracturing fluids. (a) Top-view model from the XOY perspective where the red line represents the trajectory of the steel casing well; (b) perspective view from the XOZ angle illustrating the trajectory of the well casing [blue curve], the fracturing fluid model [yellow ellipsoid], and the receiver [black square]; (c) XOZ plane grid model at Y = 0 m; (d) perspective view from the XOY angle depicting the trajectory of the well casing [blue curve], the fracturing fluid model [yellow ellipsoid], and receiver [black square]; (e) XOY plane grid model at Z = −1000 m; (f) perspective view from the YOZ angle showcasing the trajectory of the well casing [blue curve], the fracturing fluid model [yellow ellipsoid], and the receiver [black squares]; (g) YOZ plane grid model at X = 500 m.

away from the wellhead to $(-300, 0, 0)$ m, with an interval of 20 m. The dimensions, positions, and conductivities of the fracturing fluids were kept constant, as shown in Fig. 7 (a).
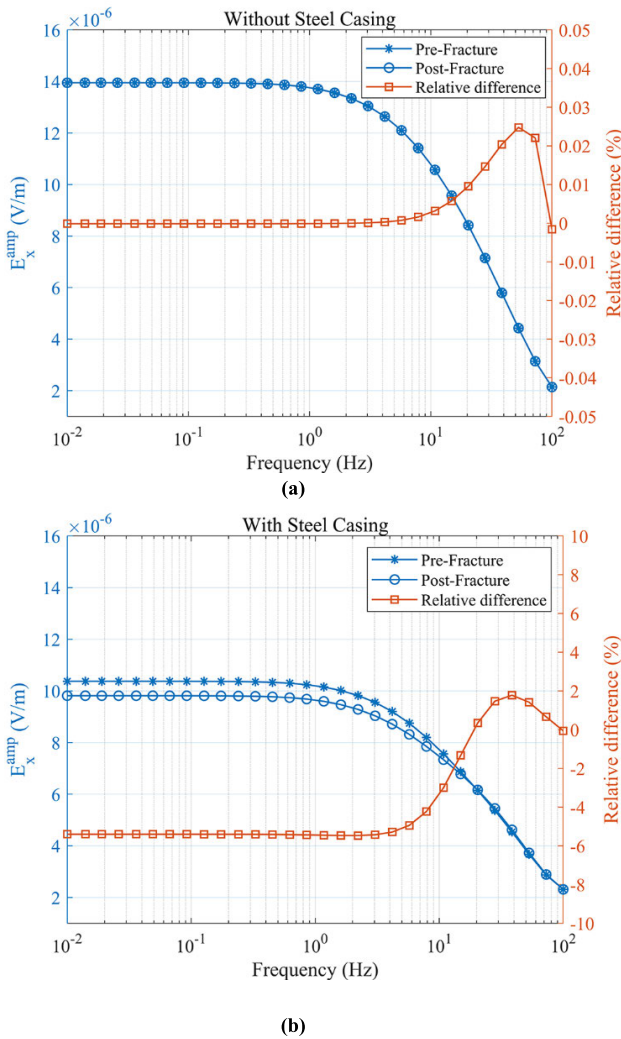
FIGURE 8. The pre- and post-fracture E_x^{amp}, and their relative difference at position $(500, 0, 0)$ m. (a) The result at different frequencies without steel casing; (b) the result at different frequencies with steel casing.

FIGURE 9. The pre- and post-fracture E_x^{amp} and their relative difference at position $(500, 0, 0)$ m. (a) The result at different distances without steel casing; (b) the result at different distances with steel casing.

The receiver was positioned at $(500, 0, 0)$ m. The transmitters were performed at 2 Hz.

The results shown in Fig. 9 demonstrate that, regardless of the presence of the underground steel casing, the surface E_x^{amp} at post-fracture was consistently lower than that at pre-fracture. In scenarios without an underground steel casing, the relative difference between E_x^{amp} pre- and post-fracture stands was $-10^{-3}\%$ (Fig. 9 (a)). However, when an underground steel casing was present, the relative difference shifted to -5.8% (Fig. 9 (b)). This demonstrates that closer proximity between the transmitter of the CSEM system and the wellhead provides a more favorable advantage in identifying underground fracturing fluids.

The investigation of the relationship between the relative difference in the surface E_x^{amp} and the migration of fracturing fluid is also essential for the implementation of the land CSEM method in realistic field surveys. Thus, in the high-resistivity cap layer model illustrated above, we simulated the
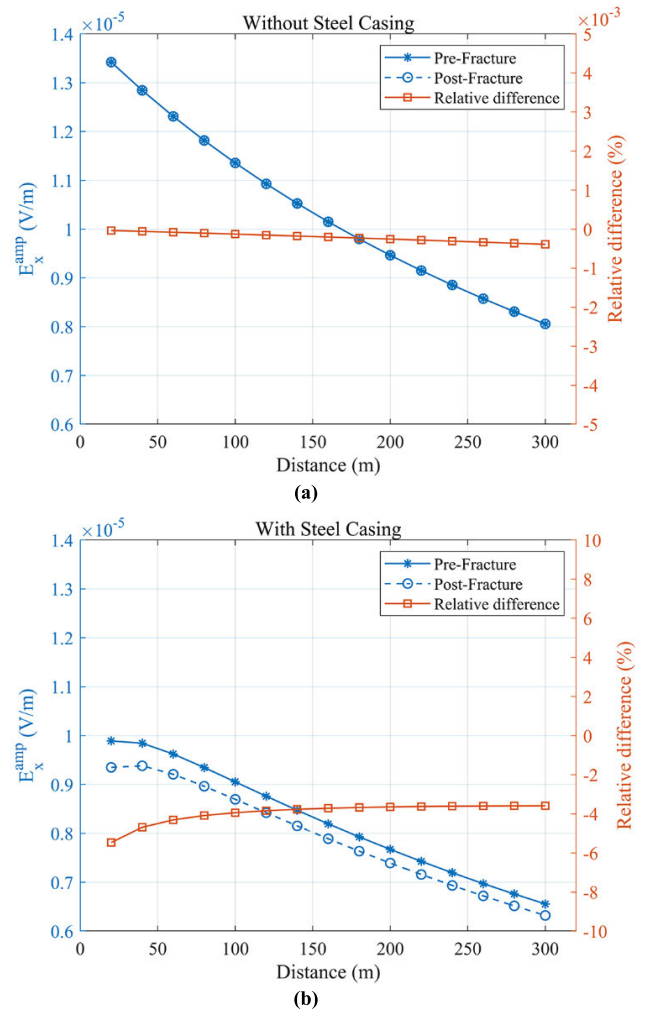
movement of the fracturing fluid in four distinct directions (in the YOZ plane: $+Z$, $-Z$, $+Y$, $-Y$) within the subsurface space (Fig. 10 (a), Fig. 10 (c), Fig. 10 (e), and Fig. 10 (g)). For the three clusters of fracturing fluid within a single fracturing stage, the dimensions and electrical conductivity of the ellipsoidal fracturing models remained constant, with variations occurring solely in their positions and central point coordinates. Table 1 lists the central coordinates of the ellipsoidal fracturing fluid models at the final moment of migration. The 5000 m-length horizontal electrical dipole source, with electrodes A $(-20, 0, 0)$ m and B $(-5020, 0, 0)$ m, had a 1 A current at a frequency of 2 Hz. The surface X-component electric field receiver grid, uniformly spaced at 40 m, extends from 40 m to 800 m in the X-direction and from -320 m to 320 m in the Y-direction. To ensure consistency in the simulation outcomes, four models employed the same set of mesh cells, and the total number was 979,608.

The results depicted in Fig. 11 indicate that the injection of fracturing fluid from perforations in the steel casing into

TABLE 1. Migration parameters for elliptical fracturing fluid model in a single stage with 3 clusters.

Migration Plane		YOZ			
Migration Direction		+Z	+Y	−Z	−Y
The First Ellipsoid	X(m)	460	460	460	460
Fracturing Fluid	Y(m)	0	100	0	−100
Model	Z(m)	-900	−1000	−1100	−1000
The Second	X(m)	500	500	500	500
Ellipsoid Fracturing	Y(m)	0	100	0	-100
Fluid Model	Z(m)	-900	−1000	−1100	−1000
The Third Ellipsoid	X(m)	540	540	540	540
Fracturing Fluid	Y(m)	0	100	0	-100
Model	Z(m)	-900	−1000	−1100	−1000

the subsurface invariably leads to a decline in the surface E_x^{amp}. Simultaneously, the migration of the hydraulic fracturing fluid in different directions induces varying relative differences in the surface E_x^{amp} pre- and post-fracture. The movement of the fracturing fluid in the +Y, −Y, +Z, and −Z directions disrupted the symmetrical distribution trend of the relative differences of E_x^{amp}. The simulation results demonstrated that the steel casing plays a beneficial role in identifying fracturing fluids using the land CSEM method under the high-resistivity cap layer model. It is important to note that, in contrast to common knowledge in the CSEM method, the electric-field anomaly does not peak at the horizontal location of the fluid because of the involvement of steel casings.

IV. APPLICATION TO REALISTIC HEAVY OIL HYDRAULIC FRACTURING MODEL

In this section, we employ our proposed methodology to estimate the feasibility of utilizing the land CSEM method to monitor hydraulic fracturing fluids. The experimental site is in a horizontal Well K#1 in Karamay Oilfield, Xinjiang, China. The average vertical depth of the horizontal section in Well K #1 was approximately 720 m, and its horizontal length was approximately 1000 m. The equivalent edge conductivity of the casing was set to a value of 1.5×10^5 S/m. Table 2 lists the conductivity profiles derived from well log K #1. The conductivity of the air layer was 1×10^{-7} S/m. The goal of this project is to conduct hydraulic fracturing within the Carboniferous strata in the horizontal section of Well K #1 to enhance the recovery rate. It is noteworthy that the subsurface layers from 0m to 490 m generally exhibited lower resistivity, indicating the characteristics of a low-resistivity overburden. This poses significant challenges when employing electromagnetic (EM) methods for hydraulic fracturing monitoring. We conducted a feasibility analysis of the near-casing land CSEM configuration using a realistic well trajectory and resistivity model from Well K #1. Additionally, simulations were carried out to analyze the effect of the steel casing considering different frequencies, various distances between the transmitter and wellhead, and diverse migration directions of fracturing fluids.

We utilized the model presented in Table 2 to simulate E_x^{amp} at the surface receiver (500, 0, 0) m across
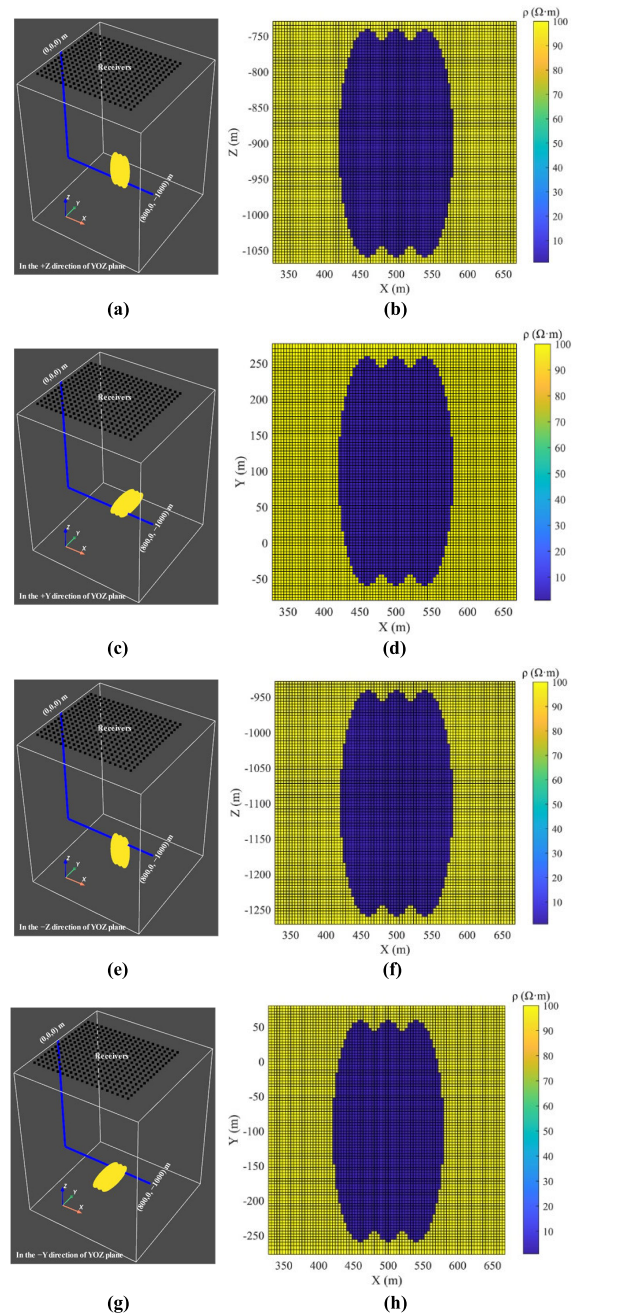

FIGURE 10. Directional fluid flow within the high-resistance cap layer model. (a) illustrate schematic spatial positions of the model after the migration of fracturing fluid towards the +Z; (b) represent slice of the grid model shown in Fig. 10 (a) at Y = 0 m; (c) illustrate schematic spatial positions of the model after the migration of fracturing fluid towards the +Y; (d) represent slice of the grid model shown in Fig. 10 (c) at Z = −1000 m; (e) illustrate schematic spatial positions of the model after the migration of fracturing fluid towards the −Z; (f) represent slice of the grid model shown in Fig. 10 (e) at Y = 0 m; (g) illustrate schematic spatial positions of the model after the migration of fracturing fluid towards the −Y; (h) represent slice of the grid model shown in Fig. 10 (g) at Z = −1000 m. In these illustrations, the blue curve represents the trajectory of the steel casing well, the yellow ellipsoid represents the fracturing fluid model, and the black squares denote receivers.

varying frequencies, subsequently computing the relative difference before and after hydraulic fracturing. In this simulation, scenarios with and without a casing within the model were included to observe the impact of the steel casing.
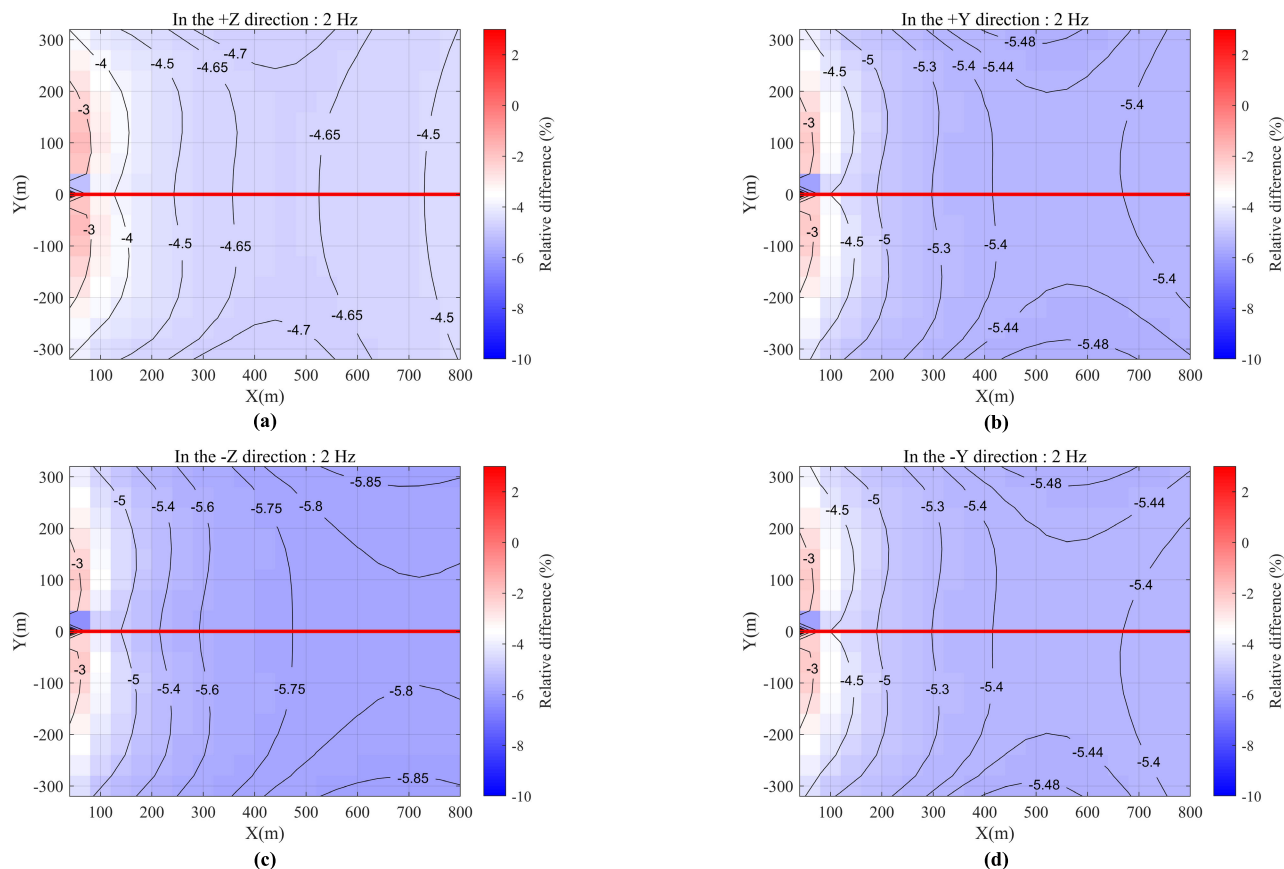
FIGURE 11. Contour map of relative differences between pre- and post-fracture at 2 Hz. (a–d) sequentially represent simulation results after the migration of fracturing fluid towards the +Z, +Y, −Z, and −Y directions in the YOZ plane. In each diagram, the red line depicts the trajectory of the steel casing well.

TABLE 2. Geoelectrical resistivity model based on K #1 log-wells.

Stratigraphy	Lithology	Burial depth (m)	Thickness (m)	Resistivity (Ω·m)	Conductivity (S/m)
Tugulu Group, Cretaceous	Gravelly Argillaceous Fine Sandstone	0-120	120	4.3	0.233
Qigu Formation, Jurassic	Gritstone	120-240	120	5.5	0.182
Xishanyao Formation, Jurassic	Mudstone	240-280	40	5	0.200
Sangonghe Formation, Jurassic	Silty Mudstone	280-360	80	5.6	0.179
Badaowan Formation, Jurassic	Argillaceous Fine Sandstone	360-450	90	6.7	0.149
Baijiantan Formation, Jurassic	Gritstone	450-460	10	15	0.067
Karamay Formation, Triassic	Silty Mudstone	460-490	30	5	0.200
Carboniferous	Gritstone	490-690	200	53.5	0.019
Carboniferous	Gritstone (Horizontal Section of Well K #1)	690-760	70	183	0.005
Carboniferous	Gritstone	760-830	70	79	0.013
Carboniferous	Gritstone	830-		110	0.009

A 5000 m-long horizontal electric dipole source, with positive electrode A at (−20, 0, 0) m and negative electrode B at (−5020, 0, 0) m, was deployed. The centers of the three horizontally arranged fracturing fluid ellipsoid models were located at (460, 0, −720) m, (500, 0, −720) m, and (540, 0, −720) m, as depicted in Fig. 12. The total number of mesh cells was 689,208. We computed the forward modeling results for 30 logarithmically spaced frequencies ranging from 0.01Hz to 100 Hz with a current of 1 A.

Based on the findings illustrated in Fig. 13 (a), it is evident that in the absence of a steel casing, the relative difference range of E_x^{amp} remains confined within −0.03% to 0.01%. When a steel casing was present, the relative difference between the pre- and post-fracturing measures ranged from −6.5% to 5% (Fig. 13 (b)). This indicates the significant effect of the steel casing, amplifying the relative difference by several hundred times, notably within realistic heavy oil fracturing models. These outcomes underscore the positive role of steel casing wells in enhancing the identification of fracturing fluids using the land CSEM method in practical modeling scenarios. The simulation results in Fig. 13 (b) provide quantitative evidence for selecting the optimal frequencies for field operation.
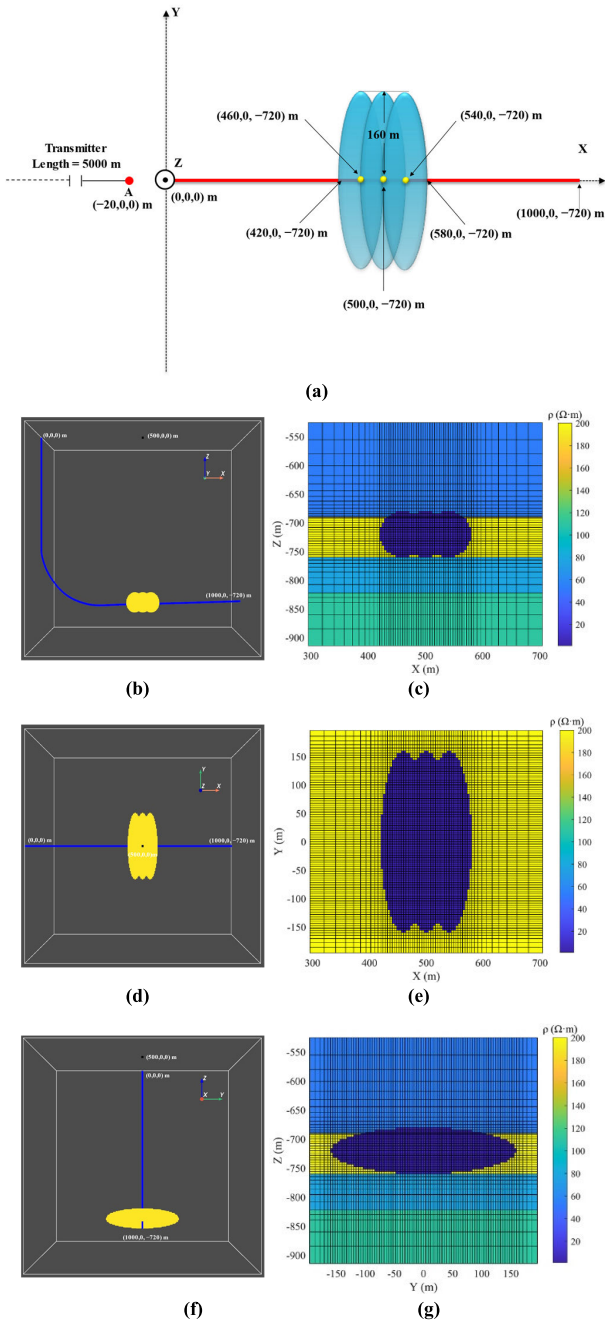
FIGURE 12. Synthetic model of realistic heavy oil hydraulic fracturing with three parallel arranged elliptical fracturing fluids. (a) Top-view model from the XOY perspective where the red line represents the trajectory of the steel casing well; (b) perspective view from the XOZ angle illustrating the trajectory of the well casing [blue curve], the fracturing fluid model [yellow ellipsoid], and the receiver [black square]; (c) XOZ plane grid model at Y = 0 m; (d) perspective view from the XOY angle depicting the trajectory of the well casing [blue curve], the fracturing fluid model [yellow ellipsoid], and receiver [black square]; (e) XOY plane grid model at Z = −720 m; (f) perspective view from the YOZ angle showcasing the trajectory of the well casing [blue curve], the fracturing fluid model [yellow ellipsoid], and the receiver [black squares]; (g) YOZ plane grid model at X = 500 m.

In a similar manner, to analyze the relationship between the relative difference of E_x^{amp} at the pre- and post-fracturing moments and the distance of the transmitter from the well-head, we employed the model outlined in Table 2. The
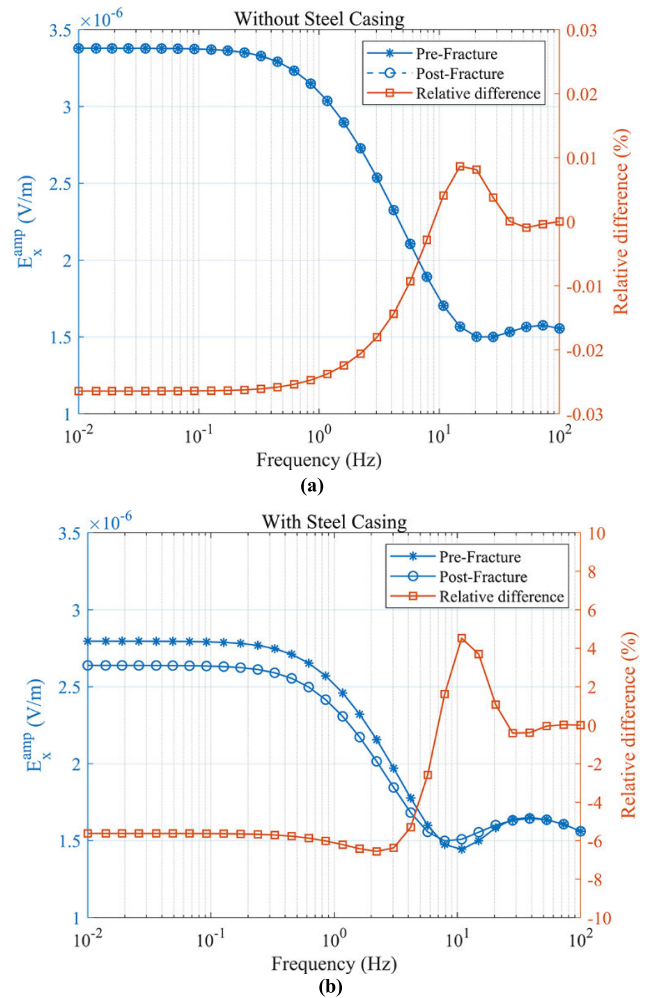

FIGURE 13. The pre- and post-fracture E_x^{amp} and their relative difference at position (500, 0, 0) m. (a) The result at different frequencies without steel casing; (b) the result at different frequencies with steel casing.

parameters and positions of the fracturing fluid models, and the length of the transmitter remained constant, as illustrated in Fig. 12. The receiver was positioned at coordinates (500, 0, 0) m, and observations were conducted at 3 Hz. The transmitter electrode A is initially positioned at (−20, 0, 0) m and gradually moves away from the wellhead to (−300, 0, 0) m with an interval of 20 m.

In the absence of a steel casing well, the relative difference between the pre- and post-hydraulic fracturing approaches approximately $-10^{-2}\%$ (Fig. 14 (a)). Clearly, the presence of a steel casing well leads to the amplification in the maximum relative difference of E_x^{amp}, approaching approximately -6.5% (Fig. 14 (b)). We also observed two phenomena: first, the E_x^{amp} of post-fracturing was lower than that of pre-fracturing at all frequencies; second, the proximity of the transmitter to the wellhead correlated with a preferred larger value of the relative difference.

We utilized the low-resistivity overburden model outlined in Table 2 to examine the impact of fracturing fluid migration on the surface E_x^{amp}. The horizontal electric dipole source positive electrode (A), with a length of 5000 m, was located at
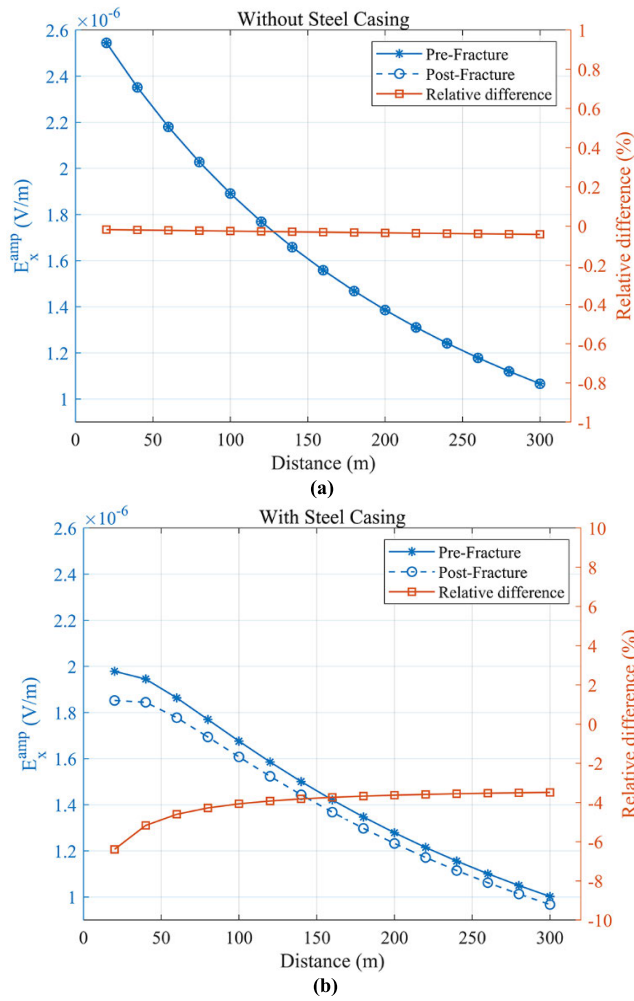
(a)

(b)

FIGURE 14. The pre- and post-fracture E_x^{amp} and the relative difference at position (500, 0, 0) m for the realistic fracturing model. (a) The result at different distances without steel casing; (b) the result at different distances with steel casing.

TABLE 3. Migration parameters for elliptical fluid model in a single-stage fracturing with 3 clusters.

Migration Plane		YOZ			
Migration Direction		+Z	+Y	−Z	−Y
The First Ellipsoid	X(m)	460	460	460	460
Fracturing Fluid	Y(m)	0	100	0	−100
Model	Z(m)	-620	−720	−820	−720
The Second	X(m)	500	500	500	500
Ellipsoid Fracturing	Y(m)	0	100	0	-100
Fluid Model	Z(m)	-620	−720	−820	−720
The Third Ellipsoid	X(m)	540	540	540	540
Fracturing Fluid	Y(m)	0	100	0	-100
Model	Z(m)	-620	−720	−820	−720

(−20, 0, 0) m, while the negative electrode B was positioned at (−5020, 0, 0) m. The current was 1 A, and the transmitter frequency was 3 Hz. The surface X-component electric field receiver grid, uniformly spaced at 40 m, extends from 40 m to
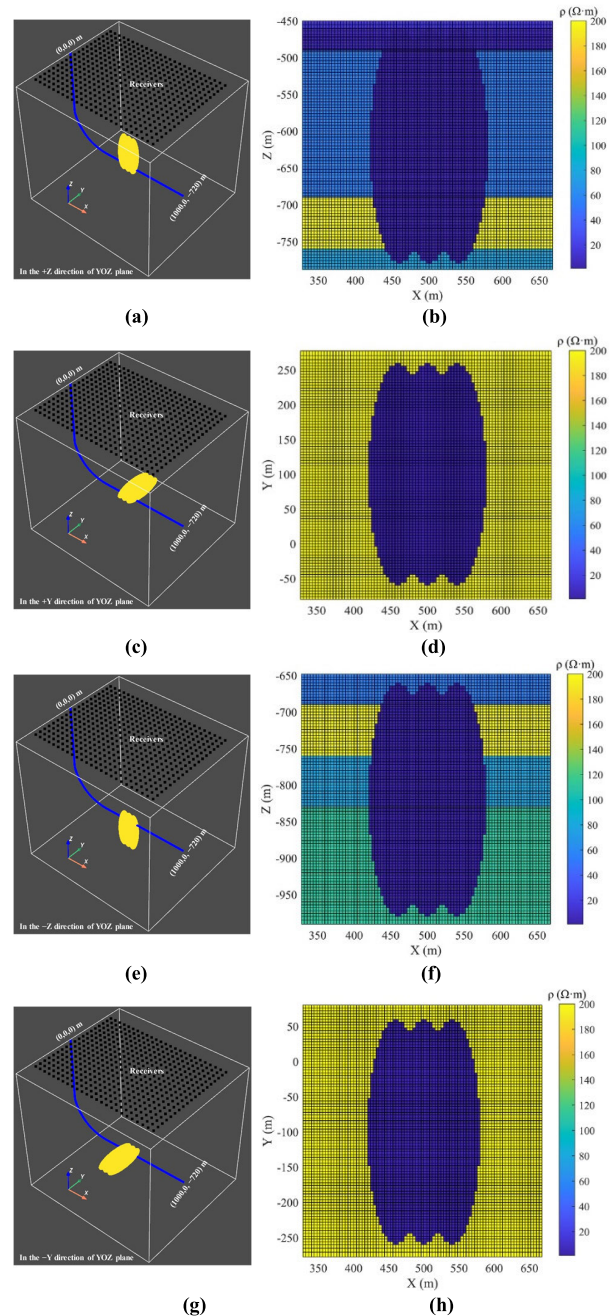

FIGURE 15. Directional fluid flow within the realistic heavy oil hydraulic fracturing model. (a) illustrate schematic spatial positions of the model after the migration of fracturing fluid towards the +Z; (b) represent slice of the grid model shown in Fig. 15 (a) at Y = 0 m; (c) illustrate schematic spatial positions of the model after the migration of fracturing fluid towards the +Y; (d) represent slice of the grid model shown in Fig. 15 (c) at Z = −720 m; (e) illustrate schematic spatial positions of the model after the migration of fracturing fluid towards the −Z; (f) represent slice of the grid model shown in Fig. 15 (e) at Y = 0 m; (g) illustrate schematic spatial positions of the model after the migration of fracturing fluid towards the −Y; (h) represent slice of the grid model shown in Fig. 15 (g) at Z = −720 m. In these illustrations, the blue curve represents the trajectory of the steel casing well, the yellow ellipsoid represents the fracturing fluid model, and the black squares denote receivers.

1000 m in the X-direction, and from −360 m to 360 m in the Y-direction. In a single-stage fracturing operation, the dimensions and conductivity of the three-cluster fracturing fluid
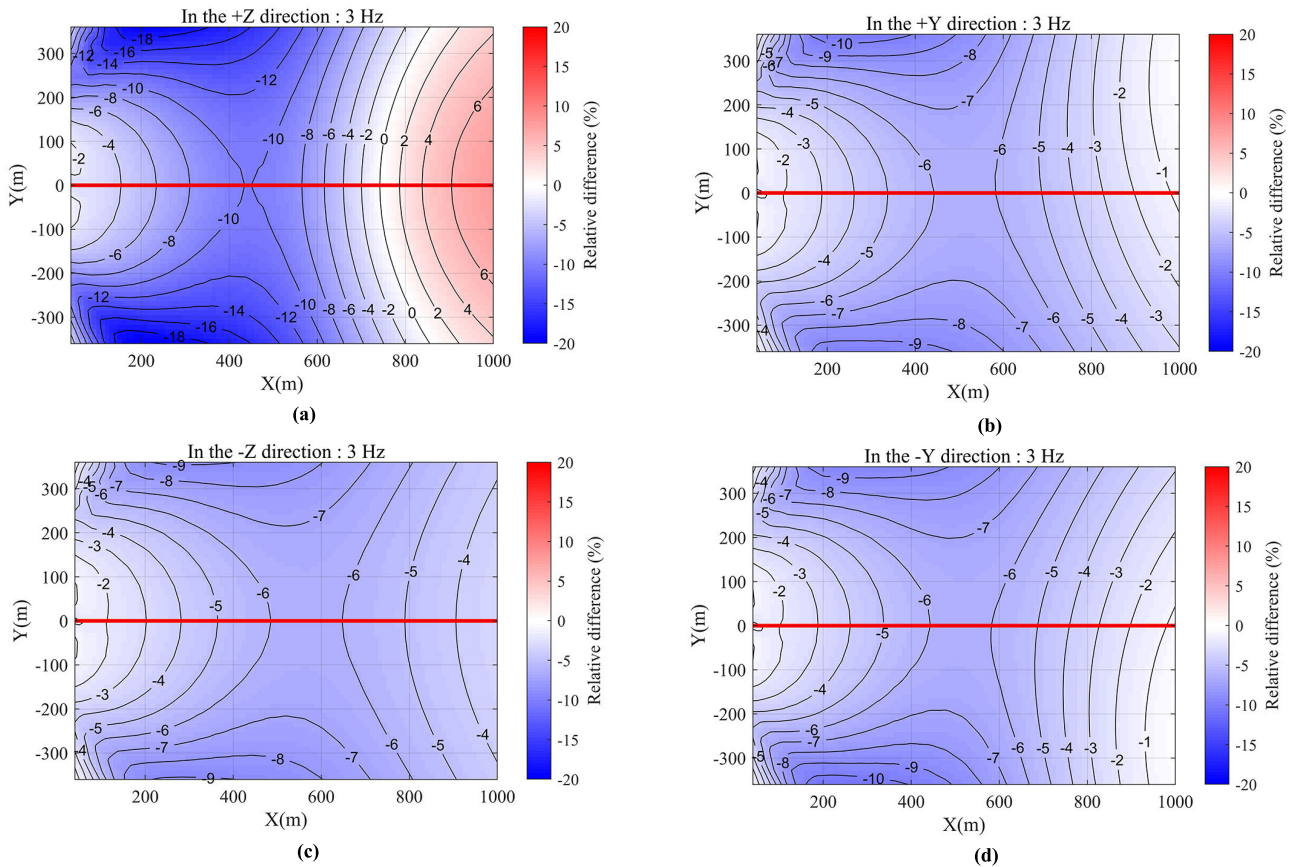
FIGURE 16. Contour map of relative differences between pre- and post-fracture at 3 Hz. (a–d) sequentially represent simulation results after the migration of fracturing fluid towards the +Z, +Y, −Z, and −Y directions in the YOZ plane. In each diagram, the red line depicts the trajectory of the steel casing well.

models were consistent with those depicted in Fig. 12; the only alterations were in the coordinates of the center. In the illustrated low-resistivity overburden model, we conducted simulations to track the movement of fracturing fluid in four specific directions within the subsurface space, namely, in the YOZ plane: +Z, +Y, −Z, and −Y (refer to Fig. 15 (a), Fig. 15 (c), Fig. 15 (e), and Fig. 10 (g)). Each simulation was conducted using an identical mesh comprising of 998,816 mesh cells. Table 3 presents the central coordinates of the elliptical fracturing fluid model at the final time step of the migration.

The simulation results confirm that the migration of the hydraulic fracturing fluid in the subsurface +Z, +Y, −Z, and −Y direction of YOZ plane significantly influences the relative difference distribution trend of the surface E_x^{amp} pre- and post-fracture (as shown in Fig. 16). In this scenario, when the hydraulic fracturing fluids migrated in the +Z and −Z directions of YOZ plane within the formation, the relative differences in the surface E_x^{amp} exhibited a symmetric distribution around the well K #1 trajectory. However, when the hydraulic fracturing fluids migrated in the +Y and −Y directions of YOZ plane, the symmetry of the relative differences along the well K #1 trajectory was disrupted. The application of our approach demonstrates the feasibility of conducting hydraulic fracturing

monitoring in a realistic geologic setting using the method proposed in this study and employing the land CSEM method.

V. CONCLUSION
This study employed a 3D FVM algorithm to conduct numerical simulations of land CSEM responses with near-casing transmitters and surface observations above horizontal wells. This study aims to analyze the feasibility of monitoring subsurface hydraulic fracturing fluids. The comparative validation results between our method and COMSOL under various model configurations demonstrated the accuracy of the approach. In this study, using a 1-A current and a 1 m long receiving electrode separation, signals in the range of approximately 2×10^{-6} V to 11×10^{-6} V were obtained within the synthetic model of high-resistivity cap layers. In a realistic heavy oil fracturing model, observed signals in the range of approximately 1.4×10^{-6} V to 2.8×10^{-6} V were obtained. Currently, in-field surveys of land CSEM high-power transmitters are commonly employed, allowing excitation currents to exceed 100 A. This enables the actual observed signals to reach magnitudes of over 1×10^{-4} V. Taking the V8 instrument from Phoenix Geophysics in Canada as an example, at a gain of $1\times$, approximately 1 A/D count corresponds to a voltage of about 3×10^{-7} volts (2.5 V$/2^{23} \approx 0.3$ μV).

Therefore, 1×10^{-4} V corresponds to a factor of 3333 times the 1 A/D count, which significantly exceeds both the instrument's observation precision and typical noise levels. Furthermore, under the high-resistivity cap layer model and realistic heavy oil model, the relative difference between pre- and post-fracture may exceed 5%. Specifically, the relative difference in the observed signals can reach 5×10^{-6} V, which is approximately 16 times the value of the 1 A/D count $(3 \times 10^{-7}$ V).

Additionally, the injection of fracturing fluids decreases the surface electric field irrespective of the presence of a subsurface steel casing. Moreover, steel casings play a crucial role in land CSEM systems for hydraulic fracturing monitoring by not only changing the distribution of surface electric field responses, but also drastically amplifying the relative difference between pre- and post-fracture. The high-resistivity cap-layer model simulation results confirmed the validity of this conclusion. In the realistic heavy oil fracturing model, the presence of a steel-cased well also significantly altered the surface electric field responses owing to fracturing fluid migration in the subsurface space. This validated the feasibility of employing the land CSEM method for hydraulic fracturing monitoring under a low-resistivity overburden. However, the validity of our method is based on a certain magnitude of resistivity difference between fracturing fluid and surrounding rock. Hence, it is necessary to appropriately consider the influence of a steel casing well when utilizing the land CSEM method and optimizing the survey parameters for effective monitoring of hydraulic fracturing.

REFERENCES

[1] S. Constable and L. J. Srnka, "An introduction to marine controlled-source electromagnetic methods for hydrocarbon exploration," *Geophysics*, vol. 72, no. 2, pp. 3–12, Mar. 2007.

[2] B. Siemon, A. V. Christiansen, and E. Auken, "A review of helicopter-borne electromagnetic methods for groundwater exploration," *Near Surf. Geophys.*, vol. 7, nos. 5–6, pp. 629–646, Jul. 2009.

[3] S. Constable, "Ten years of marine CSEM for hydrocarbon exploration," *Geophysics*, vol. 75, no. 5, pp. 67–81, Sep. 2010.

[4] Q. Di, G. Xue, C. Yin, and X. Li, "New methods of controlled-source electromagnetic detection in China," *Sci. China Earth Sci.*, vol. 63, no. 9, pp. 1268–1277, Jun. 2020.

[5] Q. Di, R. Zhu, G. Xue, C. Yin, and X. Li, "New development of the electromagnetic (EM) methods for deep exploration," *Chin. J. Geophys.*, vol. 62, no. 6, pp. 2128–2138, Jun. 2019.

[6] N. Black and M. S. Zhdanov, "Active geophysical monitoring of hydrocarbon reservoirs using EM methods," in *Handbook of Geophysical Exploration: Seismic Exploration*. London, U.K.: Elsevier, 2010, pp. 135–159.

[7] Z. He, Z. Hu, Y. Gao, L. He, C. Meng, and L. Yang, "Field test of monitoring gas reservoir development using time-lapse continuous electromagnetic profile method," *Geophysics*, vol. 80, no. 2, pp. 127–134, Mar. 2015.

[8] L.-J. Yan, X.-X. Chen, H. Tang, X.-B. Xie, L. Zhou, W.-B. Hu, and Z.-X. Wang, "Continuous TDEM for monitoring shale hydraulic fracturing," *Appl. Geophys.*, vol. 15, no. 1, pp. 26–34, Mar. 2018.

[9] A. Rey, E. Bhark, K. Gao, A. Datta-Gupta, and R. Gibson, "Streamline-based integration of time-lapse seismic and production data into petroleum reservoir models," *Geophysics*, vol. 77, no. 6, pp. 73–87, Nov. 2012.

[10] B. Peterson and A. Gerhardt, "Pluto gas field: Successful placement of an infill well based on 4D seismic monitoring," *Lead. Edge*, vol. 39, no. 7, pp. 464–470, Jul. 2020.

[11] Y. Hu, D. Yang, Y. Li, Z. Wang, and Y. Lu, "3-D numerical study on controlled source electromagnetic monitoring of hydraulic fracturing fluid with the effect of steel-cased wells," *IEEE Trans. Geosci. Remote Sens.*, vol. 60, 2022, Art. no. 4504210.

[12] M. Commer, G. M. Hoversten, and E. S. Um, "Transient-electromagnetic finite-difference time-domain earth modeling over steel infrastructure," *Geophysics*, vol. 80, no. 2, pp. 147–162, Mar. 2015.

[13] L. J. Heagy and D. W. Oldenburg, "Electrical and electromagnetic responses over steel-cased wells," *Lead. Edge*, vol. 41, no. 2, pp. 83–92, Feb. 2022.

[14] J. Li, J. Liu, J. Xue, R. Guo, H. Chen, and R. Liu, "A feasibility study of CSEM in geological advance forecast with horizontal casing well," *Minerals*, vol. 12, no. 5, p. 638, May 2022.

[15] L. J. Heagy and D. W. Oldenburg, "Impacts of magnetic permeability on electromagnetic data collected in settings with steel-cased wells," *Geophys. J. Int.*, vol. 234, no. 2, pp. 1092–1110, Mar. 2023.

[16] D. F. Rucker, J. B. Fink, and M. H. Loke, "Environmental monitoring of leaks using time-lapsed long electrode electrical resistivity," *J. Appl. Geophys.*, vol. 74, no. 4, pp. 242–254, Aug. 2011.

[17] D. F. Rucker, M. H. Loke, M. T. Levitt, and G. E. Noonan, "Electrical-resistivity characterization of an industrial site using long electrodes," *Geophysics*, vol. 75, no. 4, pp. 95–104, Jul. 2010.

[18] Y.-Y. Zhang, D.-J. Liu, Q.-H. Ai, and M.-J. Qin, "3D modeling and inversion of the electrical resistivity tomography using steel cased boreholes as long electrodes," *J. Appl. Geophys.*, vol. 109, pp. 292–300, Oct. 2014.

[19] E. Haber, C. Schwarzbach, and R. Shekhtman, "Modeling electromagnetic fields in the presence of casing," in *Proc. SEG Tech. Program Expanded Abstr.*, Houston, TX, USA, Sep. 2016, pp. 959–964.

[20] P. Zhang, Y. Brick, and M. M. Sharma, "Numerical study of an electrode-based resistivity tool for fracture diagnostics in steel-cased wellbores," *Geophysics*, vol. 83, no. 2, pp. 41–48, Mar. 2018.

[21] E. S. Um, M. Commer, G. A. Newman, and G. M. Hoversten, "Finite element modelling of transient electromagnetic fields near steel-cased wells," *Geophys. J. Int.*, vol. 202, no. 2, pp. 901–913, Jun. 2015.

[22] C. J. Weiss, D. F. Aldridge, H. A. Knox, K. A. Schramm, and L. C. Bartel, "The direct-current response of electrically conducting fractures excited by a grounded current source," *Geophysics*, vol. 81, no. 3, pp. 201–210, May 2016.

[23] T. C. Johnson and D. Wellman, "Accurate modelling and inversion of electrical resistivity data in the presence of metallic infrastructure with known location and dimension," *Geophys. J. Int.*, vol. 202, no. 2, pp. 1096–1108, Jun. 2015.

[24] M. Ronczka, C. Rücker, and T. Günther, "Numerical study of long-electrode electric resistivity tomography—Accuracy, sensitivity, and resolution," *Geophysics*, vol. 80, no. 6, pp. 317–328, Nov. 2015.

[25] E. Haber, C. Schwarzbach, W. Wilhelms, and M. McMillan, "A multiscale approach for casing modeling," in *Proc. 79th EAGE Conf. Exhib.*, Paris, France, 2017, pp. 1–5.

[26] C. Schwarzbach and E. Haber, "Improved upscaling of steel-cased wells through inversion," in *Proc. SEG Tech. Program Expanded Abstr.*, Dallas, TX, USA, Aug. 2018, p. 5520.

[27] A. L. Ramirez, R. L. Newmark, and W. D. Daily, "Monitoring carbon dioxide floods using electrical resistance tomography (ERT): Sensitivity studies," *J. Environ. Eng. Geophys.*, vol. 8, no. 3, pp. 187–208, Sep. 2003.

[28] D. Yang, "RESnet: 3D direct-current resistivity simulation using the equivalent resistor network circuit," *Geophysics*, vol. 89, no. 2, pp. 41–51, Mar. 2024, doi: 10.1190/geo2023-0336.1.

[29] C. J. Weiss, "Finite-element analysis for model parameters distributed on a hierarchy of geometric simplices," *Geophysics*, vol. 82, no. 4, pp. 155–167, Jul. 2017.

[30] Y. Li and D. Yang, "Electrical imaging of hydraulic fracturing fluid using steel-cased wells and a deep-learning method," *Geophysics*, vol. 86, no. 4, pp. E315–E332, Jul. 2021.

[31] C. J. Weiss and S. Constable, "Mapping thin resistors and hydrocarbons with marine EM methods, Part II—Modeling and analysis in 3D," *Geophysics*, vol. 71, no. 6, pp. 321–332, Nov. 2006.

[32] K. Key, "1D inversion of multicomponent, multifrequency marine CSEM data: Methodology and synthetic studies for resolving thin resistive layers," *Geophysics*, vol. 74, no. 2, pp. 9–20, Mar. 2009.

YAO LU received the B.S. degree in geophysics and the M.S. degree in exploration geophysics from Yangtze University, Wuhan, China, in 2011 and 2014, respectively. He is currently pursuing the Ph.D. degree with China University of Geosciences, Beijing, China.

Since 2014, he has been a Geophysical Engineer with the Department of Gravity Magnetics and Electric (GME) and Geochemical Surveys, Bureau of Geophysical Prospecting (BGP) Inc., China National Petroleum Corporation (CNPC), Zhuozhou, China. His research interests include electrical and electromagnetic exploration and fracturing fluid monitoring.

HANDONG TAN received the Ph.D. degree in geophysics from China University of Geosciences, Beijing, China, in 2000.

He is currently a Professor with the School of Geophysics and Information Technology, China University of Geosciences. His research interests include numerical simulation and inversion of electromagnetic methods, joint inversion of geophysical data, and the application of geophysical prospecting.

DIKUN YANG received the B.S. and M.S. degrees in geophysics from China University of Geoscience, Wuhan, China, in 2005 and 2008, respectively, and the Ph.D. degree in geophysics from the Geophysical Inversion Facility, University of British Columbia (UBC), Vancouver, BC, Canada, in 2014.

From 2014 to 2017, he was a Postdoctoral Researcher and a Teaching Fellow with UBC. In 2018, he was a NSERC Postdoctoral Fellow with the Lamont-Doherty Earth Observatory, Columbia University, Palisades, NY, USA. Since then, he has been an Assistant Professor with the Department of Earth and Space Sciences, Southern University of Science and Technology, Shenzhen, China. His research interests include electrical and electromagnetic exploration methods, geophysical inverse problems, geophysical applications in resource, environmental, and engineering problems.

ZHIGANG WANG received the bachelor's degree in geophysics from China University of Geosciences, Wuhan, China, in 1996, and the master's and Ph.D. degrees in earth survey and information technology from China University of Geosciences, Beijing, China, in 2004 and 2007, respectively.

He is currently a Senior Geophysical Expert with BGP. In 2011, he was a Visiting Scholar and studied with the Consortium for Electromagnetic Modeling and Inversion (CEMI), University of Utah, Salt Lake, UT, USA. His research interests include the 3-D forward of controlled-source electromagnetic (CSEM) and electromagnetic fracturing monitoring.

YUNJIAN YANG received the B.S. degree in applied geophysics from China University of Geosciences, Wuhan, China, in 1997, and the M.S. and Ph.D. degrees in geophysics from Chengdu University of Technology, Chengdu, China, in 2006.

He is currently with BGP Inc., CNPC, and is also a BGP Senior Geophysical Expert. His research interest includes electrical exploration and applications.

LIANGJUN YAN received the Ph.D. degree from the Department of Earth Sciences, Zhejiang University, Hangzhou, China, in 2002.

He is currently a Professor with Yangtze University, Wuhan, China; the Director of the Key Laboratory of Exploration Technologies for Oil and Gas Resources, Ministry of Education, Wuhan; and the Vice Director of the Key Laboratory of Geophysical Prospecting, CNPC, Wuhan. His research interests include electromagnetic prospecting theory and applications in hydrocarbon and mineral resource exploration.

WEI WAN received the B.S. and M.S. degrees from Yangtze University, Wuhan, China, in 2012 and 2015, respectively, and the Ph.D. degree from Peking University, Beijing, China, in 2019.

He is currently a Lecturer with the East China University of Technology, Nanchang, China. His research interests include frequency domain controlled-source electromagnetic methods and applications.

HANBING WANG received the B.S. degree in geophysics and the M.S. degree in exploration geophysics from China University of Geosciences, Beijing, China, in 2011 and 2014, respectively, where he is currently pursuing the Ph.D. degree.

His research interests include computational electromagnetics and geophysical inverse problems.

• • •